

Te Vacancy-Driven Anomalous Transport in ZrTe_5 and HfTe_5

Elizabeth A. Peterson,¹ Christopher Lane,¹ and Jian-Xin Zhu^{1,2}

¹*Theoretical Division, Los Alamos National Laboratory, Los Alamos, NM 87545, USA*

²*Center for Integrated Nanotechnologies, Los Alamos National Laboratory, Los Alamos, NM 87545, USA*

The strongly sample-dependent anomalous transport properties observed in the layered Dirac materials ZrTe_5 and HfTe_5 are known to strongly correlate with the presence of Te vacancies. One particular phenomenon, a negative longitudinal magnetoresistance (NLMR), has been widely speculated to be a signature of broken chiral symmetry, which serves as a hallmark of chiral anomaly in these materials. However, the role of electronic structure in the microscopic mechanism behind the transport properties of these materials, most importantly their sample dependence, is poorly understood. This prompts the question as to whether the NLMR is a genuine signature of the chiral anomaly or if the transport properties in ZrTe_5 and HfTe_5 are merely artifacts of other factors, like structural disorder. In this work, the effect of Te vacancies on the electronic structure of ZrTe_5 and HfTe_5 is investigated via first-principles calculations to garner insight into how they may modulate the transport properties of these materials. Te vacancies serve two purposes: modification of the cell volume via effective compressive strain and also production of local changes to the electronic structure. The reorganization of the electronic structure near the Fermi energy indicates that Te vacancies can rationalize conflicting reports in spectroscopic and transport measurements that have remained elusive in prior first-principles studies. These results show that Te vacancies contribute, at least in part, to the anomalous transport properties of ZrTe_5 and HfTe_5 but, critically, do not eliminate the possibility of a genuine manifestation of the chiral anomaly in these materials.

INTRODUCTION

Theoretical predictions of quantum anomalies, symmetry breaking that occurs when moving from classical field theories to quantum field theories, originated in the fields of particle and cosmological physics [1–4]. As experimental verification of predicted quantum anomalies at the relevant length and energy scales of particle and cosmological physics is generally challenging or simply intractable, the possibility of observing quantum anomalies in experimentally accessible condensed matter systems has engendered a great deal of excitement. In the case of three-dimensional (3D) Dirac and Weyl semimetals, a chiral anomaly is characterized by an imbalance in right- and left-handed chiral fermions in the presence of an applied magnetic field. The resulting chiral current may be induced by application of parallel electric and magnetic fields producing an anomalous contribution to the conductivity [4–17]. This manifests as a negative longitudinal magnetoresistance (NLMR), an experimental signature of the chiral anomaly. In recent years the layered 3D Dirac materials ZrTe_5 and HfTe_5 have garnered attention as material platforms that potentially host a chiral anomaly [12, 13, 18]. These materials exhibit a number of anomalous transport properties, including a Lifshitz transition as a function of temperature and a negative longitudinal magnetoresistance [12, 13, 17–24]. This NLMR is suggested to be evidence of the chiral anomaly in these materials [12, 13, 18]. However, NLMR is not sufficient to prove the presence of a chiral anomaly, as it may arise from alternative sources such as current jetting or defects [10, 25, 26]. Lacking a robust microscopic description of the source of the anomalous

transport properties in ZrTe_5 and HfTe_5 , it is as yet unclear if these materials exhibit a genuine chiral anomaly. Further, there is widespread controversy in the characterization of the topological nature of these materials; different experiments report different topological phases, including topological insulating and Dirac semimetallic states [12, 18–20, 23, 27–33].

The sample dependence of the topological [24, 32, 34–36] and transport [21, 24, 37, 38] properties of ZrTe_5 and HfTe_5 are well documented. Crystal growth by different methods, such as flux growth and chemical vapor transport (CVT), or different preparation processes utilizing the same method, may produce samples with different lattice constants and different (off-)stoichiometries. One suspected culprit for this variability is the production of different types and concentrations of point defects, including Te vacancies and Te interstitials. The variability in topological and transport properties is further surmised to depend on sample unit cell volume.

Topological phase transitions from a strong topological insulator, to a Dirac semimetal, to a weak topological insulator are theoretically predicted to occur with increasing volume [24, 32–36]. Recent experimental and theoretical results using angle-resolved photoemission spectroscopy (ARPES) and first-principles calculations rationalize the observed sample dependence of topological phases by reporting that Te vacancies are a source of chemical pressure, or internal strain, altering the volume of ZrTe_5 and HfTe_5 [24].

The Lifshitz transition (experimentally characterized by a change from p-type to n-type carriers and from metallic to semiconducting to metallic character with decreasing temperature as measured through Hall and longitudinal conductivity, respectively) that is widely fea-

tured in the literature on ZrTe_5 and HfTe_5 does not occur in all samples [21, 24, 37, 38]. In fact, Te deficiency appears to be critical to the observation of the Lifshitz transition at all. Experimental studies of stoichiometric and Te-deficient ZrTe_5 and HfTe_5 consistently show that the anomalous longitudinal resistivity peak only occurs in Te-deficient samples; samples that are highly stoichiometric exhibit a monotonic insulator-like increasing resistivity down to low temperatures [21, 37]. Concomitantly, the change in the sign of the Hall resistivity was measured to correlate with Te-deficiency as well [37].

Outstanding discrepancies between low temperature spectroscopic and transport measurements of ZrTe_5 and HfTe_5 suggest that the significance of Te vacancies evinces richer physics including, but not limited to, volume effects. Below the Lifshitz transition temperature, Hall conductivity measurements indicate that the primary carriers in these materials are electrons, suggesting the conduction band must be populated [13, 20, 21, 23, 37]. While most reported ARPES measurements show that as temperature decreases the Fermi energy shifts downward into the valence band at the Γ point, suggesting the primary carriers are holes [12, 30, 31]; one ARPES study observed that as temperature decreases the Fermi energy shifts upward into the conduction band in the neighborhood of the Γ point suggesting the primary carriers are electrons, consistent with Hall conductivity measurements [35]. This study went on to measure the full Brillouin zone (BZ), identifying electron pockets far from the BZ center. Electronic structure calculations on pristine ZrTe_5 and HfTe_5 do not predict any portion of the conduction band dipping below the Fermi energy, an apparent contradiction. Moreover, ARPES measurements generally suggest the Dirac point is centered at the Γ point while electronic structure calculations of the pristine materials generally place the Dirac point along the Γ -Y high-symmetry line (or Γ -Z depending on convention) [12, 23, 24, 30, 31, 35, 37].

The observation that the Lifshitz transition and NLMR occur only when Te vacancies are present strongly indicates that Te vacancies serve as more than just a source of effective strain in altering the electronic structure and transport properties of ZrTe_5 and HfTe_5 . However, a comprehensive picture of the effect of Te vacancies on the electronic structure of these materials remains to be fully demonstrated. This microscopic picture is critical to disentangling and addressing two questions: (a) to what extent can the conflicting transport and spectroscopic measurements be rationalized by Te vacancies? and (b) is the NLMR observed in these materials actually a signature of a chiral anomaly or merely an artifact of structural disorder? In this work, the first of these questions is addressed and a preliminary assessment of the second is put forward. Here, first-principles density functional theory (DFT) calculations of the electronic structure of ZrTe_5 and HfTe_5 in the presence of

Te vacancies offer insight into the role that Te vacancies play in modulating the electronic structure of these materials. These calculations reveal that while Te vacancies do indeed serve as a source of chemical pressure, or effective strain, they also significantly modify the electronic structure of ZrTe_5 and HfTe_5 . The resulting modifications are interpreted in light of the diversity of reported experimental measurements and offer a common thread rationalizing seemingly conflicting measurements. They also leave open the possibility that a chiral anomaly does indeed occur in these materials.

ELECTRONIC STRUCTURE CALCULATIONS

ZrTe_5 and HfTe_5 are layered materials with one-dimensional chains of HfTe_8 polyhedra along the \mathbf{a} axis connected by Te-Te bonds along the \mathbf{c} axis. These ac-planes are bound by vdW dispersion forces along the \mathbf{b} axis, as shown in **Figure 1(a)**. The lattice constants of ZrTe_5 and HfTe_5 are similar, as shown in Table S1. They have three symmetrically distinct Te sites, as shown in Figure 1(b). Prior experiments suggest that Te vacancies form readily on sites 2 and 3 in ZrTe_5 [37], however the calculated formation energies of Te vacancies on each site indicate that a vacancy on site 1 is the most favorable, in agreement with recent work [24]. The DFT calculated formation energies for Te vacancies on each site are shown in Table II. They are all relatively high compared to average thermal energy k_bT (~ 26 meV) at room temperature, ranging from 77-98 meV/atom. Nonetheless, under high temperature or non-equilibrium synthesis conditions a finite population of Te vacancies would still be expected to form. Notably, the relative formation energy differences between different vacancy sites are on the order of 10-20 meV/atom, meaning that a mixture of vacancy types should be present even though site 1 is the most stable.

TABLE I. Lattice constants of the experimental crystal structures of ZrTe_5 and HfTe_5 from the ICSD [39, 40] and the fully geometrically relaxed crystal structures calculated using DFT with Grimme-D3 dispersion corrections.

	Source	a (Å)	b (Å)	c (Å)
ZrTe_5	ICSD	3.987	14.530	13.724
	DFT	4.026	14.793	13.636
HfTe_5	ICSD	3.968	14.455	13.691
	DFT	4.000	14.711	13.596

Band Structures

The band structures of pristine ZrTe_5 and HfTe_5 (calculated with DFT at the GGA-PBE level of theory) are

TABLE II. Defect formation energies and changes in the volume and lattice constants for ZrTe_5 and HfTe_5 with Te vacancies at each symmetrically distinct site. Changes in the volume and lattice constants are for the fully relaxed defect structure and reported relative to the volume and lattice constants of the fully relaxed pristine crystal structure.

	V_{Te}	Site	E_f (meV/atom)	ΔV (%)	Δa (%)	Δb (%)	Δc (%)
ZrTe_5	1		83.1	-0.14	-0.10	0.00	-0.03
	2		88.2	-1.42	-1.01	-0.07	-0.35
	3		97.6	-1.02	-0.19	0.00	-0.83
HfTe_5	1		77.0	-0.08	-0.12	+0.06	-0.02
	2		83.5	-1.42	-1.09	-0.03	-0.31
	3		94.8	-1.10	-0.27	+0.11	-0.93

both characterized by a Dirac point at the Fermi energy that opens into a narrow band gap between the Γ and Y high-symmetry points due to spin-orbit coupling (SOC) as shown in **Figure 2(a,e)** and **Figure 3(a,e)** (see Supporting Information **Figure S1** for band structures without SOC). The PBE+SOC calculated indirect band gaps of pristine ZrTe_5 and HfTe_5 are 27 meV and 24 meV respectively. When Te vacancies are introduced, the electronic structure calculated with SOC looks very similar for both ZrTe_5 and HfTe_5 . This is likely a reflection of the very close similarity in lattice parameters between the two isostructural materials.

The PBE+SOC band structures for Te vacancies at site 1 (Figure 2(b,f) and Figure 3(b,f)) are quite similar to the pristine cases except with (i) the direct band gap at the Dirac point shifted from being along the Γ -Y high-symmetry line to being exactly at the Γ point and (ii) a decrease of the conduction band (CB) energy below the Fermi level along the Z-U and R-T high-symmetry lines. In ZrTe_5 , the Fermi energy still lies within the Dirac point gap while in HfTe_5 the Fermi energy cuts through the valence band (VB) near the Dirac point at Γ . Te vacancies at site 2 (Figure 2(c,g) and Figure 3(c,g)) shift the Fermi energy below the VB top at the Dirac point and also shift the CB below the Fermi energy in several more regions of the Brillouin zone (BZ). Te vacancies at site 3 (Figure 2(d,h) and Figure 3(d,h)) shift the CB and VB in opposite directions both towards the Fermi energy.

The electron and hole pockets introduced near the Fermi energy by each type of Te vacancy indicate that a combination of hole- and electron-like carriers should exist at low temperatures. Te vacancies at site 1 produce a strong excess of electron-like carriers, while vacancies at site 2 and 3 produce a more equal mix of hole- and electron-like carriers (see **Figure S3** in the Supporting Information for more details). As Te vacancies at site 1 are the most stable and should proliferate at the highest concentrations, these results support the observation of n-type conductivity at low temperatures.

Figure 2(a-d) shows the band structures of pristine and Te-vacancy ZrTe_5 plotted with orbital contributions from each element indicated by purple and yellow dots for Zr and Te respectively. The band gap at the Dirac point,

circled in orange, is consistently characterized by a mix of contributions from Zr and Te orbitals. The conduction bands that shift below the Fermi energy are predominantly of Te character. One notable exception is a flat band of Zr character that lies right at the Fermi energy along the U-R high-symmetry line for Te vacancies at site 3, which would be expected to have important implications for the transport properties of this case. Nearly identical observations can be made for the band structures of HfTe_5 as shown in **Figure 3(a-d)**.

In all cases, Te vacancies make the band structures of ZrTe_5 and HfTe_5 metallic, although least dramatically for Te vacancies at site 1, the most favorable Te vacancy. The volume reduction caused by Te vacancies at site 3 is the largest ($> 1\%$), followed by site 2, while the volume reduction caused by Te vacancies at site 1 is much less dramatic ($< 0.1\%$) (see Table II for details). This explains the trend in metallicity across the band structures of each type of Te vacancy, with more effective compressive strain resulting in a more metallic band structure.

To ensure that the metallicity and reorganization of the bands at the Fermi level are not an artifact of limitations of the PBE+D3 method, the band structure of each vacancy site is calculated for HfTe_5 using lattice constants (a) fixed at the values for the pristine structures, allowing only internal coordinate relaxation, and (b) from a full geometry optimization. The band structures, reported in the Supporting Information **Figure S2**, show that volume effects only slightly alter the energies, at which the new conduction and valence band states appear near the Fermi energy, but do not qualitatively change the presence or dispersion of the new bands.

At the Γ point, the direct band gap is larger in the presence of Te vacancies than it is for the pristine crystal structures. This is consistent with recent band structure calculations of HfTe_5 under compressive strain [24] and supports the hypothesis that Te vacancies affect the electronic structure, at least in part, in a similar manner to an applied strain.

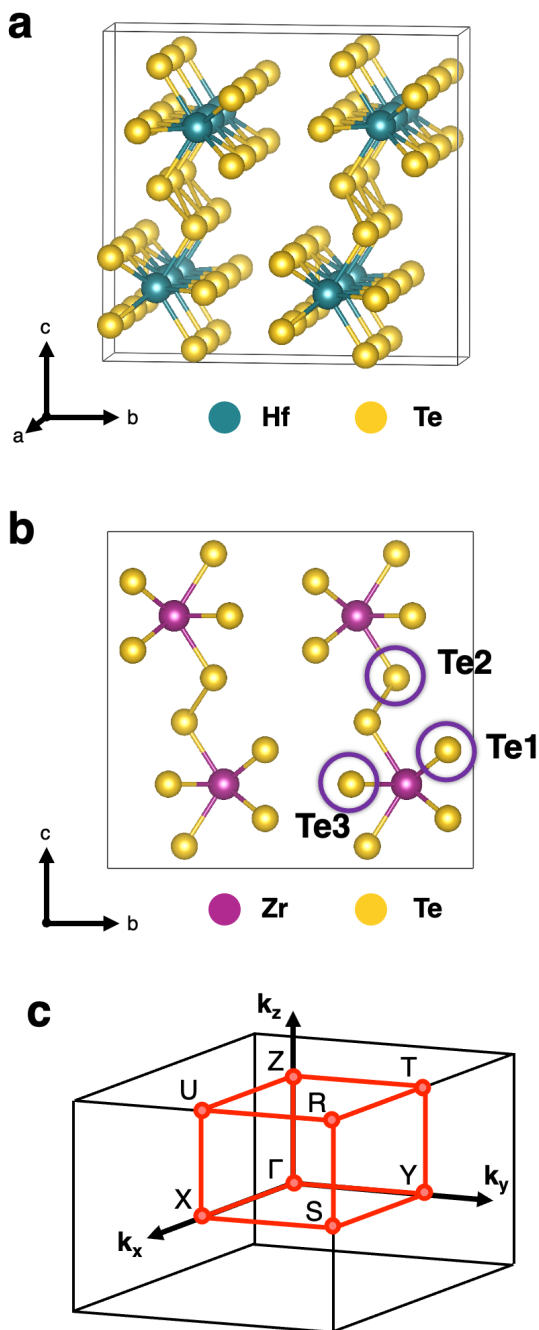


FIG. 1. (a) The conventional crystal structure of HfTe₅ characterized by Hf ion (teal) polyhedron centers each coordinated to 8 Te ions (yellow). Layers of HfTe₈ polyhedra are formed by Hf-Te bonded chains along the **a** direction and Te-Te bonded chains along the **c** directions. Layers are stacked along the **b** direction held together by vdW dispersion forces. (b) The isostructural conventional crystal structure of ZrTe₅ with Zr ions in purple and Te ions in yellow. The three symmetrically distinct Te ion sites are indicated. (c) Orthorhombic Brillouin zone with high-symmetry points used in the band structure calculations shown in Figure 2-4 marked.

Site Projected Densities of States

To better understand the source of the energy shifts and reordering of the bands near the Fermi energy, the site-projected density of states is calculated for ions in regions near the Te vacancy sites and ions in regions far from the Te vacancy sites. This makes it possible to disentangle the distinct effects of volume compression and additional states contributed by the Te vacancies. The density of states far from the Te vacancy sites should reflect only the effects of compressive strain while the density of states close to the Te vacancy sites should reflect the combined effects of compression and any additional changes to the electronic structure generated by the presence of the Te vacancy.

The local site projected density of states for the Zr and Te ions in the Zr polyhedron furthest away from the Te vacancy (Far from V_{Te}) strongly resembles the density of states of pristine ZrTe₅ (as shown in **Figure 4(a-d)**), with the exception of a notable shift in the position of the band gap for Te vacancies on site 2. Conversely, the local site projected density of states for the ions in the Zr polyhedron where the Te vacancy is located (Near V_{Te}) indicates that orbitals near the Te vacancy are the primary source of in-gap states. A similar conclusion is drawn from the site projected densities of states both near and far from the Te vacancies for HfTe₅ (**Figure 4(e-h)**).

DISCUSSION

The electronic structure calculations offer a robust avenue towards rationalizing the experimentally observed low temperature transport and spectroscopic properties of ZrTe₅ and HfTe₅, as DFT calculations correspond to zero temperature.

Near the Γ point in the electronic structure, the Fermi energy either remains in the band gap at the Dirac point or cuts through the valence band (as in the case of Te vacancies at site 2). This is consistent with most of the experimental ARPES observations near the Γ point [12, 30, 31]. However, when considering the entire Brillouin zone, it becomes clear that there is significant population of the conduction bands throughout regions of the BZ that are further away from Γ when Te vacancies are present. This is consistent with more comprehensive ARPES measurements that observed electron pockets along the Y-S high-symmetry line [35].

Resistivity measurements at low temperature in Te deficient samples report metallic conduction with electron-like carriers. The low temperature metallicity is consistent with the existence of in-gap states in the vicinity of Te vacancies. In particular, Te vacancies at sites 2 and 3 can generate flat bands near the Fermi energy from conduction bands that have shifted to lower energy, such as

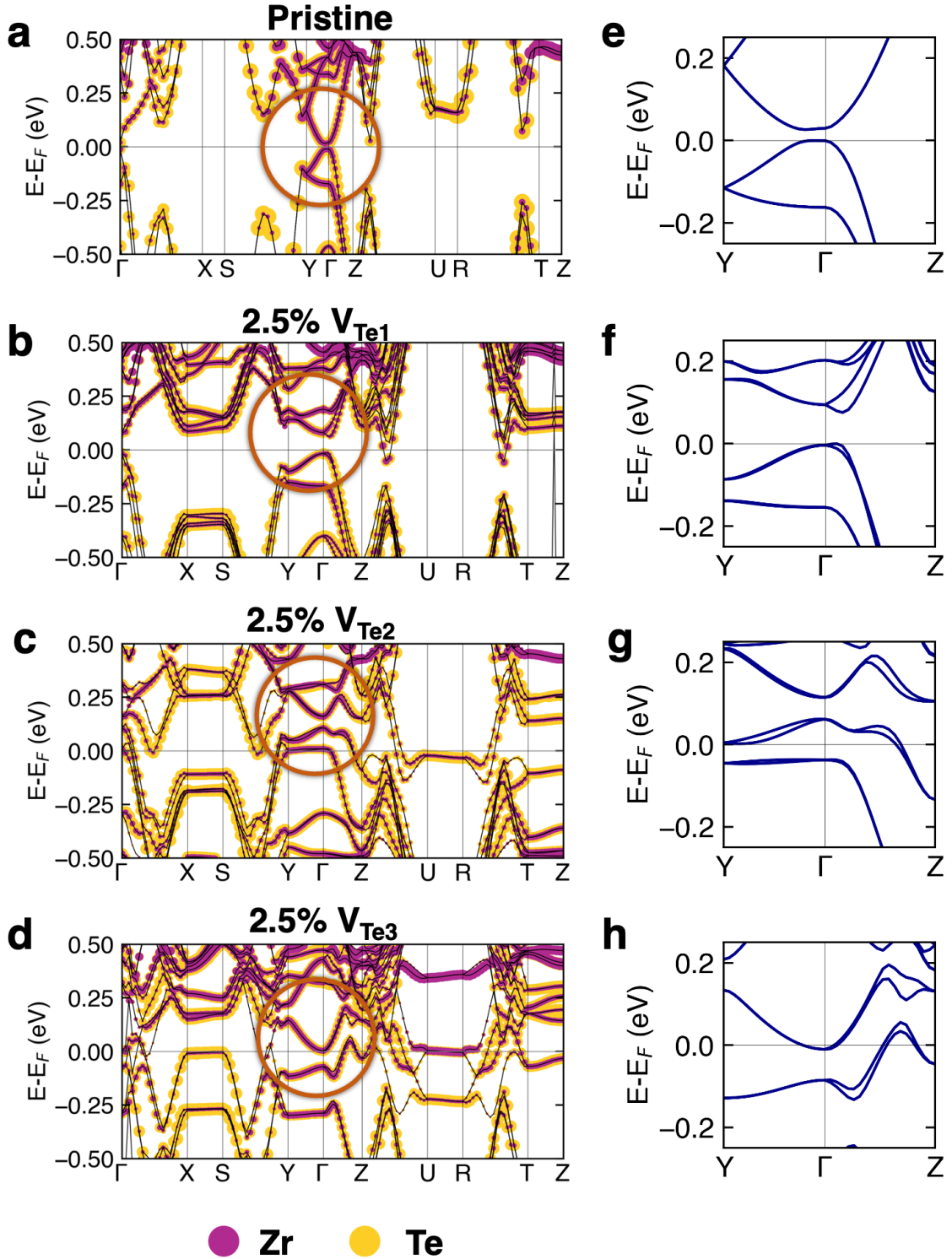


FIG. 2. The DFT+SOC band structures near the Fermi energy of ZrTe_5 in the fully relaxed geometry for the pristine crystal structure (a,e) and the cases of a neutral Te vacancy in Te site 1 (b,f), Te site 2 (c,g), and Te site 3 (d,h). High symmetry lines in the entire orthorhombic Brillouin zone shown in Figure 1c are plotted in (a-d). Zoomed-in views close to the Γ -point are plotted in (e-h).

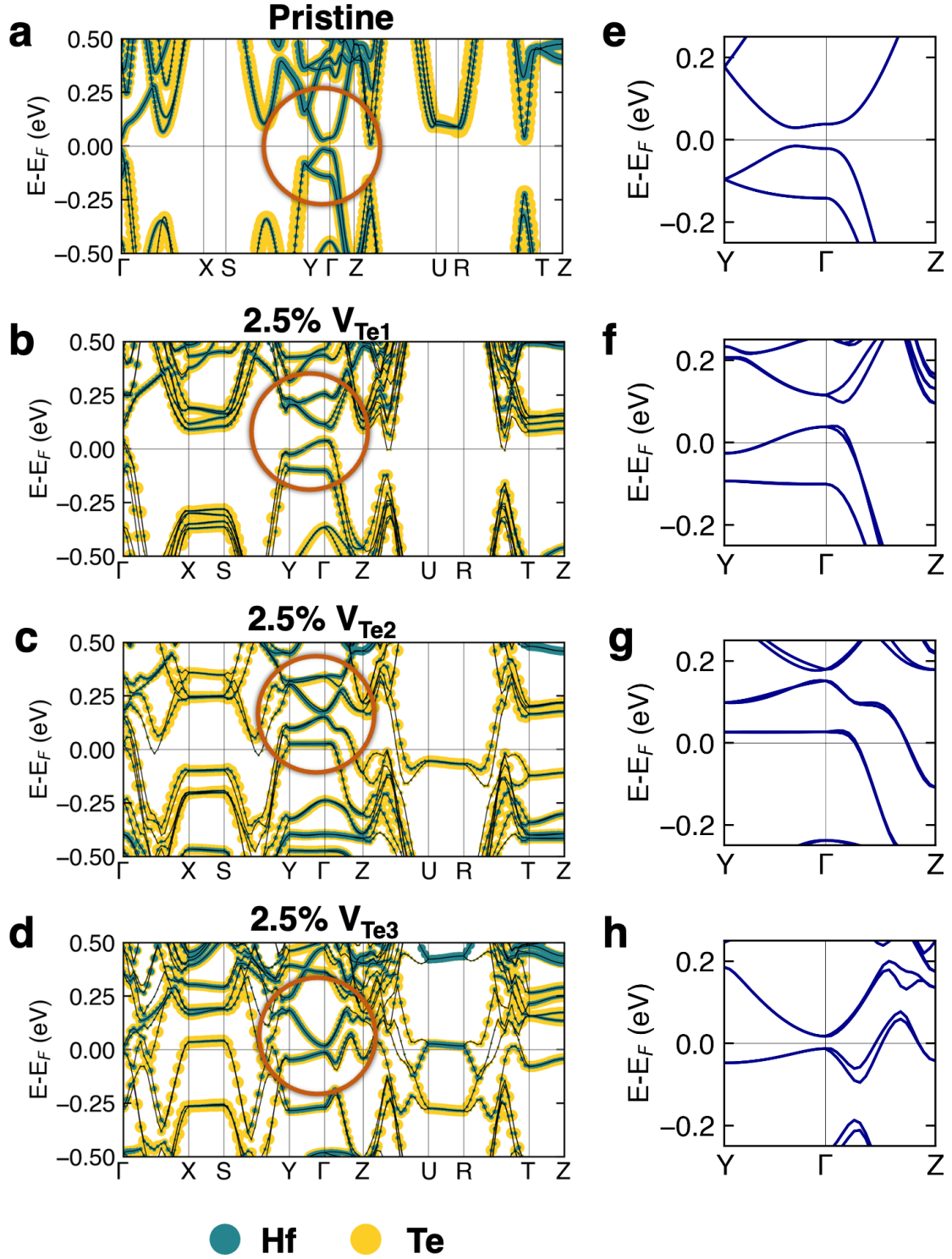


FIG. 3. Same as Figure 2 except for HfTe₅. The DFT+SOC band structures near the Fermi energy of ZrTe₅ in the fully relaxed geometry for the pristine crystal structure (a,e) and the cases of a neutral Te vacancy in Te site 1 (b,f), Te site 2 (c,g), and Te site 3 (d,h). High symmetry lines in the entire orthorhombic Brillouin zone shown in Figure 1c are plotted in (a-d). Zoomed-in views close to the Γ -point are plotted in (e-h).

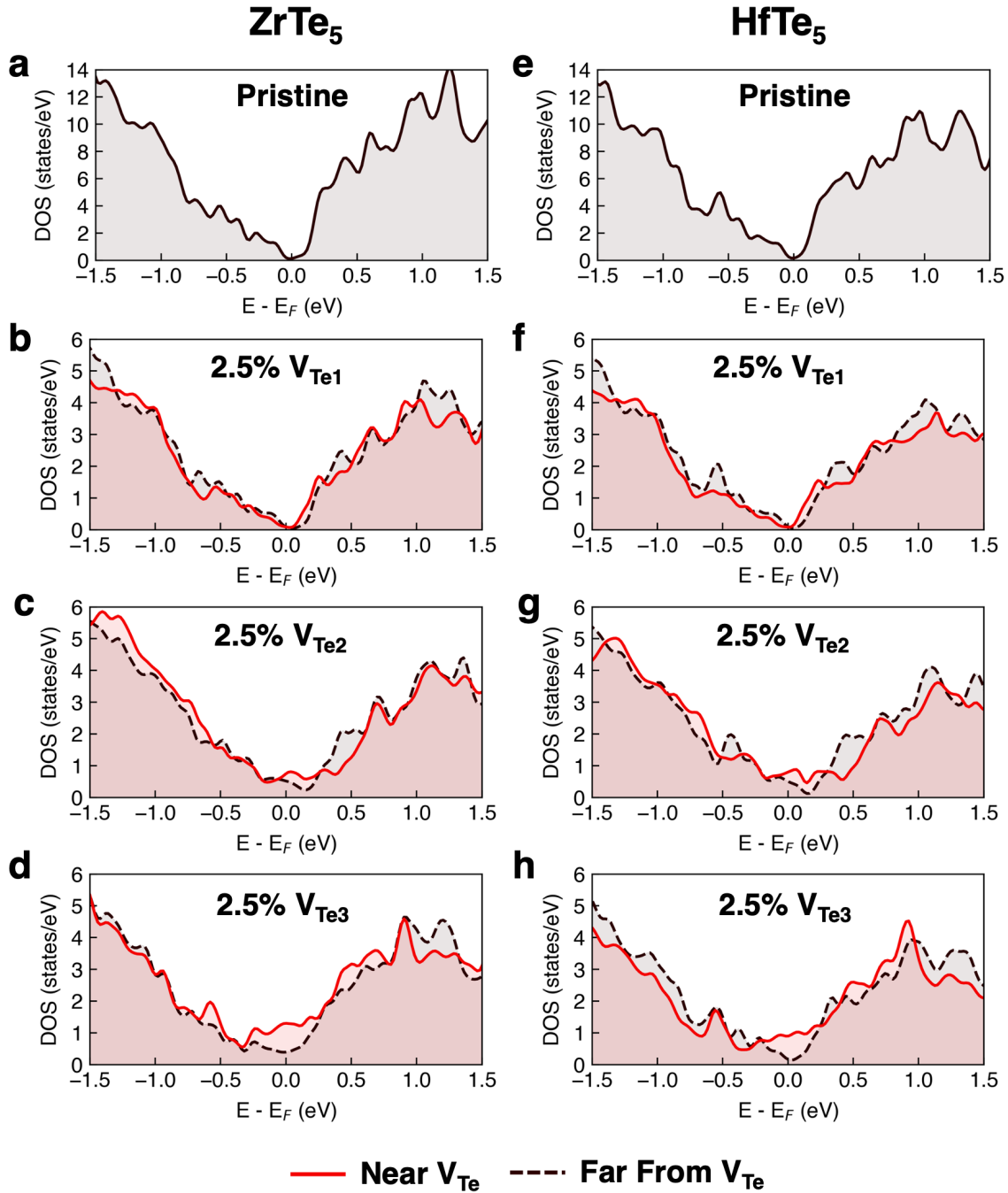


FIG. 4. The DFT+SOC densities of states for ZrTe_5 and HfTe_5 in the fully relaxed geometries for the pristine crystal structure (a,e) and for a neutral Te vacancy on Te site 1 (b,f), Te site 2 (c,g), and Te site 3 (d,h). The projected density of states is plotted for orbitals on ions in the Zr (or Hf) polyhedron where the Te vacancy is located (Near V_{Te} , solid red line) and the Zr (or Hf) polyhedron farthest from the Te vacancy (Far from V_{Te} , black dashed line).

in Figure 2(c,d) and Figure 3(c,d). From the band structure calculations, it becomes clear that a combination of populations of electron-like and hole-like carriers is to be expected at low temperature. However, flat bands

associated with valence band states appear as well. Te vacancies at site 1, which are the most stable and expected to be the most prolific, produce a strong excess of electron-like carriers, consistent with Hall resistivity

measurements that consistently observe n-type conductivity at low temperatures.

Combined, these calculations offer an explanation for the seemingly conflicting results of ARPES measurements and Hall conductivity measurements.

The production of in-gap states localized near anion vacancies is not a unique feature of Dirac materials. This is commonly observed, such as the production of in-gap flat bands spanning the entire Brillouin zone when oxygen vacancies are introduced into metal oxides [41–43]. The in-gap states produced by orbitals near the Te vacancies, however, are noteworthy in that they have a variety of dispersions near the Fermi energy, including linear crossings and flat bands along certain high symmetry lines. It is also important to note that they appear at points in the Brillouin zone far from the Γ point. The narrow gap at the Γ point that is the hallmark of massive Dirac materials is robust to the introduction of these point defects, as shown in Figure 2(e-h) and Figure 3(e-h). This robustness of the Dirac point against structural disorder is critical. It implies that the Dirac physics expected to enable a chiral anomaly could also be robust against structural disorder.

CONCLUSIONS

In this work, first-principles DFT electronic structure calculations of the layered Dirac materials ZrTe_5 and HfTe_5 with Te vacancies offer insight into the sample dependence of their experimentally observed spectroscopic and transport properties. Consistent with most low temperature ARPES measurements, Te vacancies are shown to promote both semiconducting or hole-doped behavior at the Γ point. They further promote occupation of the conduction band by shifting conduction band states towards the Fermi energy which rationalizes the n-type conductivity at low temperatures consistently reported by Hall measurements. Different combinations of Te vacancies at different concentrations are expected to produce a spectrum of electronic structure reorganizations accounting for sample-dependent reports of gapped and metallic behavior. Te vacancies affect the electronic structure and corresponding transport properties of ZrTe_5 and HfTe_5 both as a general source of effective strain and, importantly, by introducing additional states near the Fermi energy localized in the vicinity of the Te vacancy sites. Critically, the existence of the gapped Dirac point in the DFT+SOC calculations is robust to the introduction of Te vacancies. The effect of Te vacancies on the topological character of the bands at the Γ point is left to future work. However, these results suggest that the proposed mechanism of a chiral anomaly occurring in ZrTe_5 and HfTe_5 deriving from the topological nature of Dirac materials may be robust to structural disorder; moreover, this implies that the presence of defects does not eliminate the

possibility that the NLMR observed in ZrTe_5 and HfTe_5 may be a genuine signature of a quantum anomaly in experimentally accessible condensed matter systems.

CALCULATION DETAILS

First-principles calculations are performed using density functional theory (DFT) with a plane-wave basis and projector augmented wave (PAW) pseudopotentials [44] as implemented in the Vienna *ab initio* simulation package (VASP) [45, 46]. Calculations are performed in the generalized gradient approximation (GGA) as implemented by Perdew, Burke, and Ernzerhof (PBE) [47] with additional vdW dispersion forces approximately accounted for via the Grimme-D3 method [48]. The crystal structures of bulk ZrTe_5 and HfTe_5 are relaxed using a 600 eV energy cutoff and $20 \times 8 \times 8$ Γ -centered k-mesh until forces are converged to < 1 meV/Å. This method results in good agreement of the a and c lattice constants (Table S1). The out-of-plane b lattice constants are only slightly overestimated by 1.8% and 1.7% for ZrTe_5 and HfTe_5 respectively (see Table S1 for details). The band structure is calculated both with and without spin-orbit coupling (SOC) using a 500 eV energy cutoff. The density of states is calculated with SOC.

Te vacancy calculations are performed on $2 \times 1 \times 1$ supercells of bulk ZrTe_5 and HfTe_5 with a single Te ion removed, a 2.5% Te vacancy concentration. Vacancies are introduced at each of the three symmetrically distinct Te sites. Geometry optimization is performed both for fixed lattice parameters with only internal coordinates allowed to relax as well as full crystal structure relaxation. For the supercell calculations, an energy cutoff of 500 eV and a $10 \times 8 \times 8$ Γ -centered k-mesh are used. The band structure is calculated for the fully relaxed crystal structures, to capture volume effects, both with and without spin-orbit coupling (SOC) and the density of states is calculated with SOC.

The defect formation energy is calculated using

$$E_f = E_{tot}[\text{V}_{\text{Te}}] - E_{tot}[\text{pristine}] - \sum_i n_i \mu_i \quad (1)$$

where $E_{tot}[\text{V}_{\text{Te}}]$ and $E_{tot}[\text{pristine}]$ are the DFT calculated total energies of the crystal structure with a Te vacancy and the pristine crystal structure. n_i is the number of atoms of species i added or removed (in this case one Te atom) and μ_i is the chemical potential of that species, here taken from a DFT calculation of bulk Te in the trigonal P3₁21 space group as tabulated in the ICSD [49]. The standard additional terms to correct for charge effects are neglected because only neutral Te vacancies are considered [50].

ACKNOWLEDGEMENTS

This work was supported by the U.S. DOE NNSA under Contract No. 89233218CNA000001. It was supported by the Los Alamos National Laboratory (LANL) LDRD Program, and in part by the Center for Integrated Nanotechnologies, an Office of Science User Facility operated by the U.S. Department of Energy (DOE) Office of Science, in partnership with the LANL Institutional Computing Program for computational resources. Additional computations were performed at the National Energy Research Scientific Computing Center (NERSC), a U.S. Department of Energy Office of Science User Facility located at Lawrence Berkeley National Laboratory, operated under Contract No. DE-AC02-05CH11231 using NERSC award ERCAP0020494.

-
- [1] S. L. Adler, Axial-Vector Vertex in Spinor Electrodynamics, *Phys. Rev.* **177**, 2426 (1969).
- [2] J. S. Bell and R. Jackiw, A PCAC puzzle: $\pi^0 \rightarrow \gamma\gamma$ in the σ -model, *Il Nuovo Cimento A* **60**, 47 (1969).
- [3] D. Kharzeev, Parity violation in hot QCD: Why it can happen, and how to look for it, *Physics Letters B* **633**, 260 (2006).
- [4] E. Kharzeev, Dmitri, The Chiral Magnetic Effect and anomaly-induced transport, *Progress in Particle and Nuclear Physics* **75**, 133 (2014).
- [5] H. B. Nielsen and M. Ninomiya, The Adler-Bell-Jackiw anomaly and Weyl fermions in a crystal, *Physics Letters B* **130**, 389 (1983).
- [6] K. Fukushima, D. E. Kharzeev, and H. J. Warringa, Chiral magnetic effect, *Phys. Rev. D* **78**, 074033 (2008).
- [7] D. T. Son and B. Z. Spivak, Chiral anomaly and classical negative magnetoresistance of Weyl metals, *Phys. Rev. B* **88**, 104412 (2013).
- [8] X. Huang, L. Zhao, Y. Long, P. Wang, D. Chen, Z. Yang, H. Liang, M. Xue, H. Weng, Z. Fang, X. Dai, and G. Chen, Observation of the Chiral-Anomaly-Induced Negative Magnetoresistance in 3D Weyl Semimetal TaAs, *Phys. Rev. X* **5**, 031023 (2015).
- [9] J. Xiong, S. K. Kushwaha, T. Liang, J. W. Krizan, M. Hirschberger, W. Wang, R. J. Cava, and N. P. Ong, Evidence for the chiral anomaly in the Dirac semimetal Na_3Bi , *Science* **350**, 413 (2015), <https://www.science.org/doi/pdf/10.1126/science.aac6089>.
- [10] F. Arnold, C. Shekhar, S.-C. Wu, Y. Sun, R. D. dos Reis, N. Kumar, M. Naumann, M. O. Ajeesh, M. Schmidt, A. G. Grushin, J. H. Bardarson, M. Baenitz, D. Sokolov, H. Borrmann, M. Nicklas, C. Felser, E. Hassinger, and B. Yan, Negative magnetoresistance without well-defined chirality in the Weyl semimetal TaP, *Nat. Commun.* **7**, 10.1038/ncomms11615 (2016).
- [11] C.-L. Zhang, S.-Y. Xu, I. Belopolski, Z. Yuan, Z. Lin, B. Tong, G. Bian, N. Alidoust, C.-C. Lee, S.-M. Huang, T.-R. Chang, G. Chang, C.-H. Hsu, H.-T. Jeng, M. Neupane, D. S. Sanchez, H. Zheng, J. Wang, H. Lin, C. Zhang, H.-Z. Lu, S.-Q. Shen, T. Neupert, M. Z. Hasan, and S. Jia, Signatures of the Adler-Bell-Jackiw chiral anomaly in a Weyl fermion semimetal, *Nat. Commun.* **7**, 10.1038/ncomms10735 (2016).
- [12] Q. Li, D. E. Kharzeev, C. Zhang, Y. Huang, I. Pletikosić, A. V. Fedorov, R. D. Zhong, J. A. Schneeloch, G. D. Gu, and T. Valla, Chiral magnetic effect in ZrTe_5 , *Nature Phys.* **12**, 550 (2016).
- [13] H. Chi, C. Zhang, G. Gu, D. E. Kharzeev, X. Dai, and Q. Li, Lifshitz transition mediated electronic transport anomaly in bulk ZrTe_5 , *New J. Phys.* **19**, 10.1088/1367-2630/aa55a3 (2017).
- [14] S. Nandy, G. Sharma, A. Taraphder, and S. Tewari, Chiral Anomaly as the Origin of the Planar Hall Effect in Weyl Semimetals, *Phys. Rev. Lett.* **119**, 176804 (2017).
- [15] T. Nag and S. Nandy, Magneto-transport phenomena of type-I multi-Weyl semimetals in co-planar setups, *Journal of Physics: Condensed Matter* **33**, 075504 (2020).
- [16] S. Nandy, C. Zeng, and S. Tewari, Chiral anomaly induced nonlinear Hall effect in semimetals with multiple Weyl points, *Phys. Rev. B* **104**, 205124 (2021).
- [17] Q. Xie, C. Wang, S. Yan, L. Chen, J. Zheng, and W. W., Quantum oscillations and stacked quantum Hall effect in HfTe_5 , *Appl. Phys. Lett.* **120**, 10.1063/5.0084727 (2022).
- [18] G. Zheng, J. Lu, X. Zhu, W. Ning, Y. Han, H. Zhang, J. Zhang, C. Xi, J. Yang, H. Du, K. Yang, Y. Zhang, and M. Tian, Transport evidence for the three-dimensional Dirac semimetal phase in ZrTe_5 , *Phys. Rev. B* **93**, 115414 (2016).
- [19] R. Y. Chen, S. J. Zhang, J. A. Schneeloch, C. Zhang, Q. Li, G. D. Gu, and N. L. Wang, Optical spectroscopy study of the three-dimensional Dirac semimetal ZrTe_5 , *Phys. Rev. B* **92**, 075107 (2015).
- [20] Y. Liu, X. Yuan, C. Zhang, Z. Jin, Q. Narayan, C. Luo, Z. Chen, L. Yang, J. Zou, X. Wu, S. Sanvito, Z. Xia, L. Li, Z. Wang, and F. Xiu, Zeeman splitting and dynamical mass generation in Dirac semimetal ZrTe_5 , *Nature Commun.* **7**, 10.1038/ncomms1251 (2016).
- [21] Y.-Y. Lv, X. Li, L. Cao, D. Lin, S.-H. Yao, S.-S. Chen, S.-T. Dong, J. Zhou, Y. B. Chen, and Y.-F. Chen, Tunable Resistance or Magnetoresistance Cusp and Extremely Large Magnetoresistance in Defect-Engineered $\text{HfTe}_{5-\delta}$ Single Crystals, *Phys. Rev. Appl.* **9**, 054049 (2018).
- [22] W. Zhang, P. Wang, G. Gu, X. Wu, and L. Zhang, Negative longitudinal magnetothermopower in the topological semimetal ZrTe_5 , *Phys. Rev. B* **102**, 115147 (2020).
- [23] Z. Kovács-Krausz, E. Tóvári, D. Nagy, A. Márffy, B. Karpiak, Z. Tajkov, L. Oroszlány, J. Koltai, P. Nemes-Incze, S. P. Dash, P. Makk, and S. Csonka, Revealing the band structure of ZrTe_5 using multicarrier transport, *Phys. Rev. B* **107**, 075152 (2023).
- [24] N. H. Jo, O. A. Ashour, Z. Shu, C. Jozwiak, A. Bostwick, S. H. Ryu, K. Sun, T. Kong, S. M. Griffin, and E. Rotenberg, On the effects of strain, defects, and interactions on the topological properties of HfTe_5 (2023), [arXiv:2303.10836 \[cond-mat.mtrl-sci\]](https://arxiv.org/abs/2303.10836).
- [25] R. D. dos Reis, M. O. Ajeesh, N. Kumar, F. Arnold, C. Shekhar, M. Naumann, M. Schmidt, M. Nicklas, and E. Hassinger, On the search for the chiral anomaly in Weyl semimetals: the negative longitudinal magnetoresistance, *New Journal of Physics* **18**, 085006 (2016).
- [26] Y. Li, Z. Wang, P. Li, X. Yang, Z. Shen, F. Sheng, X. Li, Y. Lu, Y. Zheng, and Z.-A. Xu, Negative magnetoresistance in Weyl semimetals NbAs and NbP: Intrinsic chiral anomaly and extrinsic effects, *Front. Phys.* **12**, 10.1007/s11467-016-0636-8 (2017).

- [27] H. Weng, X. Dai, and Z. Fang, Transition-Metal Pentatelluride ZrTe_5 and HfTe_5 : A Paradigm for Large-Gap Quantum Spin Hall Insulators, *Phys. Rev. X* **4**, 011002 (2014).
- [28] R. Y. Chen, Z. G. Chen, X.-Y. Song, J. A. Schneeloch, G. D. Gu, F. Wang, and N. L. Wang, Magnetoinfrared Spectroscopy of Landau Levels and Zeeman Splitting of Three-Dimensional Massless Dirac Fermions in ZrTe_5 , *Phys. Rev. Lett.* **115**, 176404 (2015).
- [29] X.-B. Li, W.-K. Huang, Y.-Y. Lv, K.-W. Zhang, C.-L. Yang, B.-B. Zhang, Y. B. Chen, S.-H. Yao, J. Zhou, M.-H. Lu, L. Sheng, S.-C. Li, J.-F. Jia, Q.-K. Xue, Y.-F. Chen, and D.-Y. Xing, Experimental Observation of Topological Edge States at the Surface Step Edge of the Topological Insulator ZrTe_5 , *Phys. Rev. Lett.* **116**, 176803 (2016).
- [30] R. Wu, J.-Z. Ma, S.-M. Nie, L.-X. Zhao, X. Huang, J.-X. Yin, B.-B. Fu, P. Richard, G.-F. Chen, Z. Fang, X. Dai, H.-M. Weng, T. Qian, H. Ding, and S. H. Pan, Evidence for Topological Edge States in a Large Energy Gap near the Step Edges on the Surface of ZrTe_5 , *Phys. Rev. X* **6**, 021017 (2016).
- [31] L. Moreschini, J. C. Johannsen, H. Berger, J. Denlinger, C. Jozwiak, E. Rotenberg, K. S. Kim, A. Bostwick, and M. Grioni, Nature and topology of the low-energy states in ZrTe_5 , *Phys. Rev. B* **94**, 081101 (2016).
- [32] G. Manzoni, L. Gragnaniello, G. Autès, T. Kuhn, A. Sterzi, F. Cilento, M. Zacchigna, V. Enkel, I. Vobornik, L. Barba, F. Bisti, P. Bugnon, A. Margrez, V. N. Strocov, H. Berger, O. V. Yazyev, M. Fonin, F. Parmigiani, and A. Crepaldi, Evidence for a Strong Topological Insulator Phase in ZrTe_5 , *Phys. Rev. Lett.* **117**, 237601 (2016).
- [33] Z. Tajkov, D. Nagy, K. Kandrai, J. Koltai, L. Oroszlány, P. Süle, Z. E. Horváth, P. Vancsó, T. Levente, and P. Nemes-Incze, Revealing the topological phase diagram of ZrTe_5 using the complex strain fields of microbubbles, *npj Computat Mater* **8**, 10.1038/s41524-022-00854-z (2022).
- [34] Z. Fan, Q.-L. Liang, Y. B. Chen, S.-H. Yao, and J. Zhou, Transition between strong and weak topological insulator in ZrTe_5 and HfTe_5 , *Sci. Rep.* **7**, 10.1038/srep45667 (2017).
- [35] Y. Zhang, C. Wang, L. Yu, G. Liu, A. Liang, J. Huang, S. Nie, X. Sun, Y. Zhang, B. Shen, J. Liu, W. Hongming, L. Zhao, G. Chen, X. Jia, C. Hu, Y. Ding, W. Zhao, Q. Gao, C. Li, S. He, L. Zhao, F. Zhang, S. Zhang, F. Yang, Z. Wang, Q. Peng, X. Dai, Z. Fang, Z. Xu, C. Chen, and X. J. Zhou, Electronic evidence of temperature-induced Lifshitz transition and topological nature in ZrTe_5 , *Nature Commun.* **8**, 10.1038/ncomms15512 (2017).
- [36] B. Monserrat and A. Narayan, Unraveling the topology of ZrTe_5 by changing temperature, *Phys. Rev. Res.* **1**, 033181 (2019).
- [37] P. Shahi, D. J. Singh, J. P. Sun, L. X. Zhao, G. F. Chen, Y. Y. Lv, J. Li, J.-Q. Yan, D. G. Mandrus, and J.-G. Cheng, Bipolar Conduction as the Possible Origin of the Electronic Transition in Pentatellurides: Metallic vs Semiconducting Behavior, *Phys. Rev. X* **8**, 021055 (2018).
- [38] Y. Jiang, T. Zhao, L. Zhang, Q. Chen, H. Zhou, M. Ozerov, D. Smirnov, and Z. Jiang, Revealing temperature evolution of the Dirac band in ZrTe_5 via magnetoinfrared spectroscopy, *Phys. Rev. B* **108**, L041202 (2023).
- [39] H. Fjellvåg and A. Kjekshus, Structural properties of ZrTe_5 and HfTe_5 as seen by powder diffraction, *Solid State Communications* **60**, 91 (1986).
- [40] S. Furuseth, L. Brattås, and A. Kjekshus, The Crystal Structure of HfTe_5 , *Acta Chem. Scand.* **27**, 2367 (1973).
- [41] Y. Hinuma, T. Toyao, T. Kamachi, Z. Maeno, S. Takakusagi, S. Furukawa, I. Takigawa, and K.-i. Shimizu, Density Functional Theory Calculations of Oxygen Vacancy Formation and Subsequent Molecular Adsorption on Oxide Surfaces, *The Journal of Physical Chemistry C* **122**, 29435 (2018), <https://doi.org/10.1021/acs.jpcc.8b11279>.
- [42] R. Fernández-Climent, S. Giménez, and M. García-Tecedor, The role of oxygen vacancies in water splitting photoanodes, *Sustainable Energy Fuels* **4**, 5916 (2020).
- [43] L. Zhou, E. A. Peterson, M. H. Richter, Y. Lai, J. B. Neaton, and J. M. Gregoire, Fe Substitutions Improve Spectral Response of Bi_2WO_6 -Based Photoanodes, *ACS Applied Energy Materials* **5**, 15333 (2022), <https://doi.org/10.1021/acsaem.2c02964>.
- [44] G. Kresse and D. Joubert, From ultrasoft pseudopotentials to the projector augmented-wave method, *Phys. Rev. B* **59**, 1758 (1999).
- [45] G. Kresse and J. Furthmüller, Efficiency of ab-initio total energy calculations for metals and semiconductors using a plane-wave basis set, *Computational Materials Science* **6**, 15 (1996).
- [46] G. Kresse and J. Furthmüller, Efficient iterative schemes for ab initio total-energy calculations using a plane-wave basis set, *Phys. Rev. B* **54**, 11169 (1996).
- [47] J. P. Perdew, K. Burke, and M. Ernzerhof, Generalized Gradient Approximation Made Simple, *Phys. Rev. Lett.* **77**, 3865 (1996).
- [48] S. Grimme, J. Antony, S. Ehrlich, and H. Krieg, A consistent and accurate ab initio parametrization of density functional dispersion correction (DFT-D) for the 94 elements H-Pu, *The Journal of Chemical Physics* **132**, 154104 (2010), https://pubs.aip.org/aip/jcp/article-pdf/doi/10.1063/1.3382344/15684000/154104_1_online.pdf.
- [49] C. Adenis, V. Langer, and O. Lindqvist, Reinvestigation of the structure of tellurium, *Acta Crystallographica Section C* **45**, 941 (1989).
- [50] C. G. Van de Walle and J. Neugebauer, First-principles calculations for defects and impurities: Applications to III-nitrides, *Journal of Applied Physics* **95**, 3851 (2004), NoStop

Supporting Information: Te Vacancy-Driven Anomalous Transport
in ZrTe_5 and HfTe_5

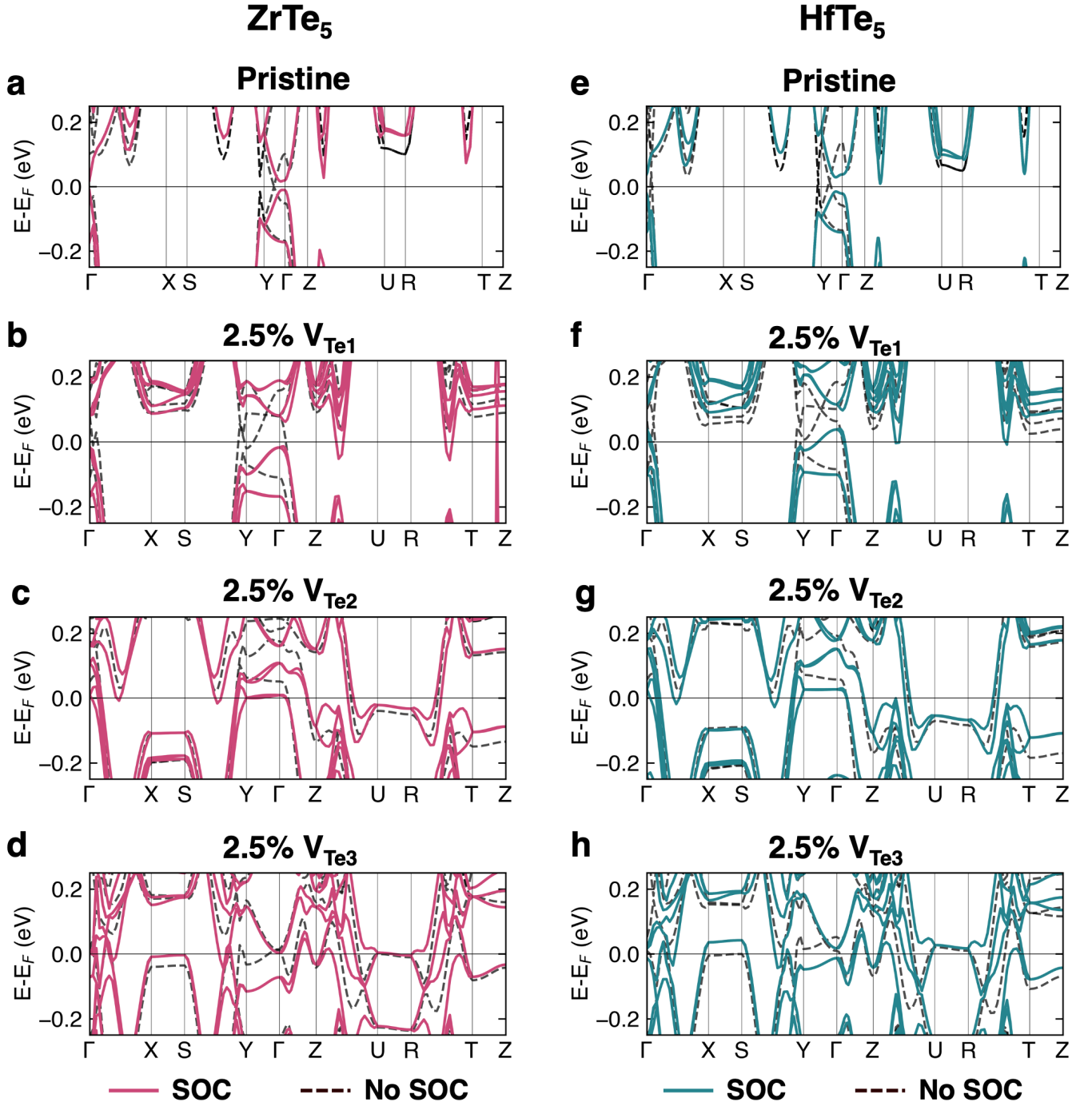


FIG. S1. The DFT band structures near the Fermi energy of $ZrTe_5$ (a-d) and $HfTe_5$ (e-h) in the fully relaxed geometries for the pristine crystal structure (a,e) and the cases of a neutral Te vacancy in Te site 1 (b,f), Te site 2 (c,g), and Te site 3 (d,h). The band structures calculated both with (solid lines) and without (dashed lines) spin-orbit coupling (SOC) are plotted to illustrate how SOC affects the band structure around the Dirac point near the Fermi energy.

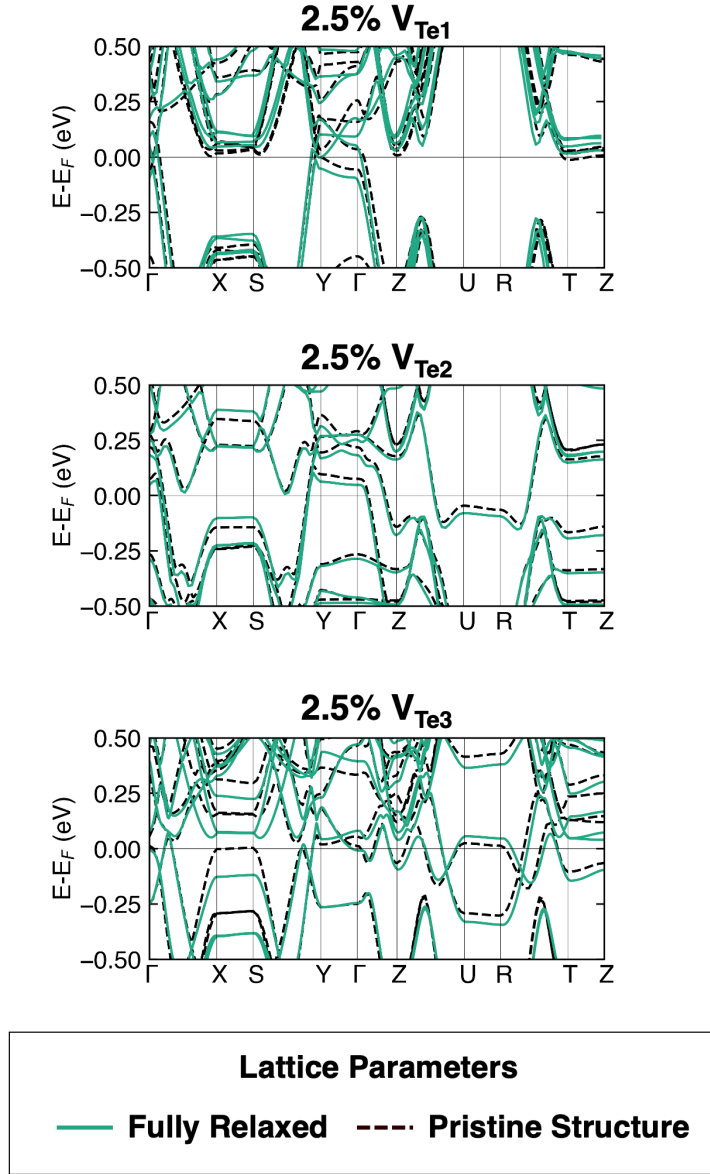


FIG. S2. Band structure of HfTe_5 with Te vacancies calculated without spin-orbit coupling. The band structure calculated with fully relaxed lattice parameters for each type of Te vacancy is shown in green solid lines. The band structure calculated with the lattice parameters fixed at the lattice parameters of pristine HfTe_5 and only internal coordinates allowed to relax is shown in black dashed lines. In each case, there are bands in different parts of the Brillouin zone that shift to different energies but their shape and dispersion remain qualitatively similar. The corresponding lattice parameters are listed in **Table S1**.

TABLE S1. Lattice constants of a $2 \times 1 \times 1$ supercell of HfTe_5 for the pristine crystal structure and the crystal structures with each type of Te vacancy relaxed using DFT with Grimme-D3 dispersion corrections. The relative changes in the lattice parameters and volume are reproduced from Table 2 in the main text.

	a (Å)	b (Å)	c (Å)	Δa (%)	Δb (%)	Δc (%)	ΔV (%)
Pristine	8.000	14.711	13.596				
V_{Te1}	7.990	14.720	13.594	-0.12	+0.06	-0.02	-0.08
V_{Te2}	7.913	14.707	13.555	-1.09	-0.03	-0.31	-1.42
V_{Te3}	7.978	14.727	13.469	-0.27	+0.11	-0.93	-1.10

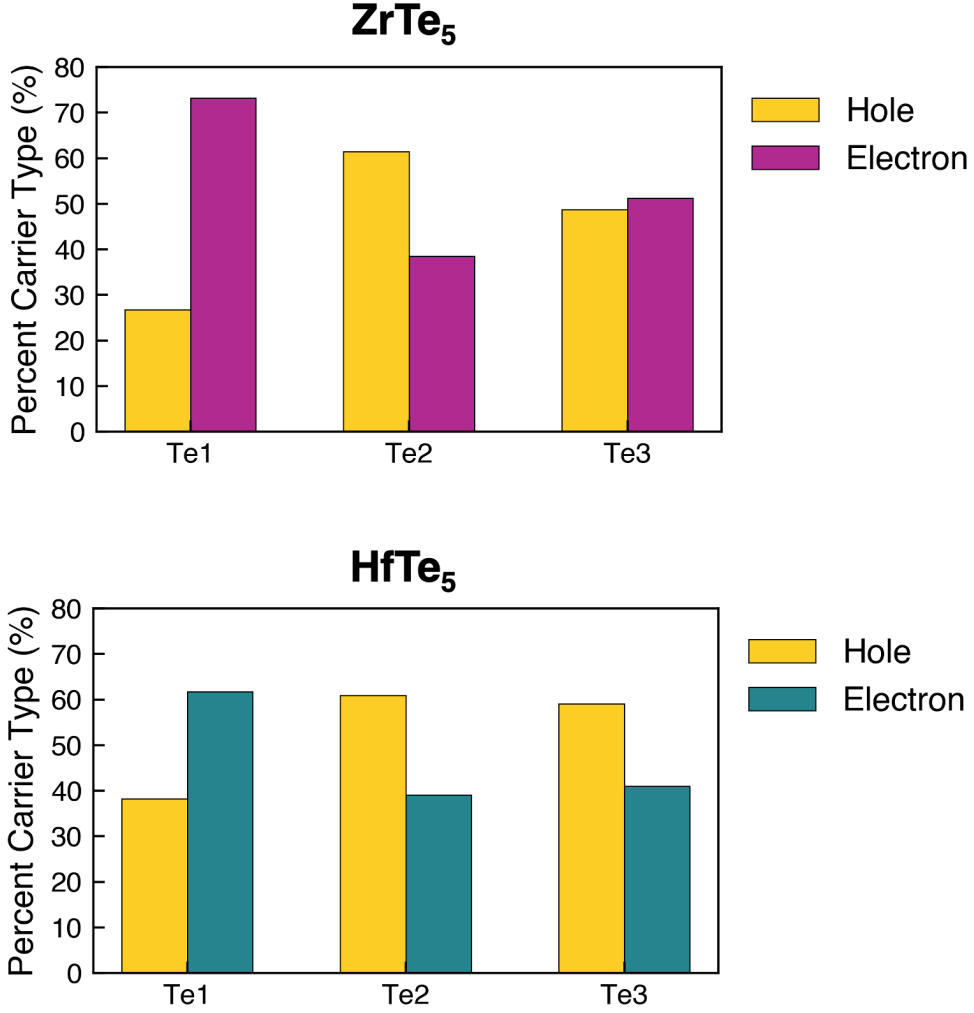


FIG. S3. Percent of states near Fermi energy that correspond to hole-like or electron-like excess carriers for each type of Te vacancy site for ZrTe_5 (top) and HfTe_5 (bottom). The absolute number of excess carriers of each type is obtained by summing the number of Kohn-Sham states above the Fermi energy for bands that are below the Fermi energy in the pristine case and by summing the number of states below the Fermi energy for bands that were above the Fermi energy in the pristine case. Te vacancies on site 1, which is the most stable and expected to proliferate at the highest concentration, produce an excess of electron-like carriers.